

Hamiltonian reconstruction via ringdown dynamics

Vincent Dumont,^{1,*} Markus Bestler,² Letizia Catalini,¹ Gabriel Margiani,¹ Oded Zilberberg,² and Alexander Eichler¹

¹*Laboratory for Solid State Physics, ETH Zürich, CH-8093 Zürich, Switzerland*

²*Department of Physics, University of Konstanz, D-78457 Konstanz, Germany*

(Dated: March 4, 2024)

Many experimental techniques aim at determining the Hamiltonian of a given system. The Hamiltonian describes the system’s evolution in the absence of dissipation, and is often central to control or interpret an experiment. Here, we theoretically propose and experimentally demonstrate a method for Hamiltonian reconstruction from measurements over a large area of phase space, overcoming the main limitation of previous techniques. A crucial ingredient for our method is the presence of dissipation, which enables sampling of the Hamiltonian through ringdown-type measurements. We apply the method to a driven-dissipative system – a parametric oscillator – observed in a rotating frame, and reconstruct the (quasi-)Hamiltonian of the system. Furthermore, we demonstrate that our method provides direct experimental access to the so-called symplectic norm of the stationary states of the system, which is tied to the particle- or hole-like nature of excitations of these states. In this way, we establish a method to unveil qualitative differences between the fluctuations around stabilized minima and maxima of the nonlinear out-of-equilibrium stationary states. Our method constitutes a versatile approach to characterize a wide class of driven-dissipative systems.

I. INTRODUCTION

The evolution of any physical system is governed by an interplay between conservative and nonconservative forces. The former are generated by a Hamiltonian ‘landscape’, i.e., the sum of all energy terms within a closed system. Understanding and controlling an experiment usually require knowledge of the system’s Hamiltonian. In a realistic setting, however, it can be difficult to compute the Hamiltonian from first principles, as it requires full insight into all microscopic constituents. Alternatively, extracting the effective Hamiltonian from a measurement provides direct access to the system dynamics even when its theoretical model is incomplete. Experimentalists therefore invest much effort in calibrating the parameters of their system in order to extract and fit their effective model [1]. A prime example is the calibration of qubits, whose gate operations rely on precise Hamiltonian estimations [2–5].

A vast majority of systems are inherently ‘open’, i.e., the dissipative coupling to an environment cannot be ignored. An open system experiences fluctuations that cause it to sample the available landscape over time. This allows estimating a system’s Hamiltonian by measuring the probability of finding it in a certain state while it is subject to fluctuations [6–13]. This method was used in experimental studies of the escape dynamics [13] and Kramers turnover [11] of a particle trapped in an optical potential, investigations of the force fields acting on these particles [14, 15], or the stability of coupled nonlinear systems [16, 17]. Probabilistic methods have the drawback that certain states are rarely explored. As such, the methods are often inadequate in situations where regions of interest (in state space) are separated by large energy

differences. In addition, these methods are insensitive to temporal correlations in the system, which pertain to the notion of causality of excitations, as quantified by e.g. out-of-time-ordered correlators [18, 19].

In the presence of dissipative coupling to an environment, it is also possible to probe a system’s Hamiltonian from its deterministic relaxation. This becomes feasible when the measured variables of interest are large enough to neglect the impact of fluctuations. By initializing a system in a well-defined state using an external drive and then turning off the drive, the system decays into a stationary state due to dissipative coupling to a large and, most often, Markovian reservoir. By measuring such a ‘ringdown’ into a stationary state (attractor), both the nonlinearity of a system close to a stable solution [20–23] and the curvature of engineered potential landscapes [24] have been measured in the absence of a drive.

In principle, such ringdown-type experiments can be extended to driven-dissipative systems. This is particularly interesting for driven nonlinear systems with multiple stable oscillation states. In a rotating frame, such oscillations can appear as stationary states within their respective basins of attraction [25, 26]. There, the system dynamics can be described by a rotating-frame quasi-Hamiltonian that, for instance, allows understanding out-of-equilibrium phase transitions [27–31] in lattices of cold atoms [24], optical oscillators [32], or cavity magnonic systems [33]. Interestingly, such systems can stabilize out-of-equilibrium phases where seemingly anti-causal excitations can manifest [29, 34]. However, to our knowledge, no full reconstruction of such a rotating-frame Hamiltonian has been reported to date.

In this paper, we demonstrate a precise and deterministic method of reconstructing the full rotating frame quasi-Hamiltonian of a driven-dissipative nonlinear system using systematic ringdown measurements. Notably, the presence of dissipation enables sampling of a large section of a Hamiltonian from a limited number of ring-

* vdumont@phys.ethz.ch

down measurements. The method provides high resolution even far from stationary solutions, where stochastic approaches typically fail. Furthermore, we obtain a direct measurement of the ‘symplectic norm’ of each solution [29, 30], providing a qualitative understanding of the different phases the system can enter, including a dissipation-stabilized maximum with hole-like quasiparticle excitations. Importantly, our method can be extended and applied to both undriven and driven-dissipative oscillating systems far from equilibrium, making it a valuable tool in many contemporary fields of physics.

We first present in Sec. II our electro-mechanical resonator system. In Sec. III, we introduce the general method to reconstruct the Hamiltonian from ringdown measurements. In Sec. IV, we reconstruct the effective Hamiltonian of our resonator in the absence of a drive – i.e., demonstrating the method for a standard damped harmonic oscillator. Then, in Sec. V, we subject the resonator to a large parametric drive to allow multiple stable oscillation solutions and compare the reconstructed rotating-frame Hamiltonian to theoretical predictions. Finally, in Sec. VI, we discuss the extraction and implications of the symplectic norm as a tool for exploring and understanding out-of-equilibrium stationary solutions.

II. ELECTROMECHANICAL DEVICE

Our device is a micro-electromechanical resonator, as illustrated in Fig. 1(a). It consists of a mechanical cantilever [35] biased with voltage $U_{\text{bias}} \approx 32$ V, used to tune the mechanical resonance frequency ω_0 [36], and which induces a Duffing non-linearity β (due to the non-linearity of the electrostatic force between the mechanical element and the electrodes [35]). To generate a weak near-resonant forcing term F , we apply a voltage $U_{\text{in}} = U_r \cos(\omega_r t + \theta)$ to one of the electrodes, where U_r is the amplitude, θ is a phase offset, and $\omega_r \approx \omega_0$. A large off-resonant voltage $U_{\text{in}} = U_p \cos(2\omega_r t + \psi)$ periodically modulates ω_0 with a modulation depth $\lambda \propto U_p$, making it possible to parametrically drive the resonator [37]. We read out the mechanical displacement x via the output voltage $U_{\text{out}} \propto x$ with a lock-in amplifier (Zurich Instruments MFLI), and forgo the proportionality coefficient for convenience (i.e., we define $U_{\text{out}} \equiv x$) [38]. The device displacement is described by the equation of motion (EOM)

$$\frac{d^2 x}{dt^2} + \omega_0^2 [1 - \lambda \cos(2\omega_r t + \psi)] x + \Gamma \frac{dx}{dt} + \beta x^3 = F, \quad (1)$$

with time t . The device has a mechanical resonance frequency $\omega_0/2\pi \approx 1.12$ MHz, energy decay rate $\Gamma/2\pi \approx 112$ Hz (quality factor $Q = \omega_0/\Gamma \approx 10^4$), and Duffing non-linearity $\beta \approx -9.9 \times 10^{16} \text{ V}^{-2}\text{s}^{-2}$. The forcing term (in units of Vs^{-2}) is $F = AU_{\text{in}}$ with a conversion factor $A \approx 16 \times 10^6 \text{ s}^{-2}$ and with the oscillator’s mass absorbed

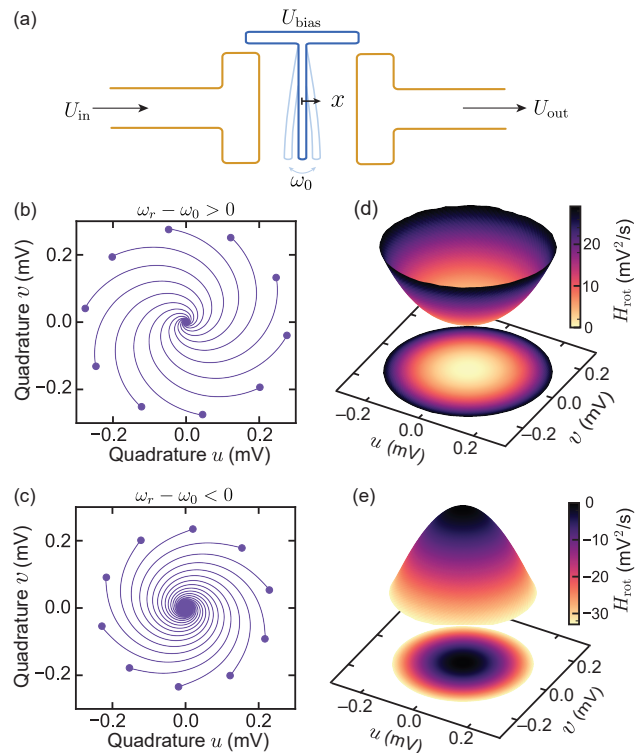


FIG. 1. Micro-electromechanical resonator and H_{rot} reconstruction of a simple damped harmonic oscillator. (a) A cantilever, biased at voltage U_{bias} , with oscillation displacement x and natural frequency ω_0 , is capacitively coupled to two conductors. Typically, an input voltage U_{in} with frequency ω_r ($2\omega_r$) can drive the mechanical resonator resonantly (parametrically), when $\omega_r \approx \omega_0$. The mechanical motion induces a voltage U_{out} , which we read out. (b) Several ringdown measurements for a few initialization points (dots) in rotating (i.e., at demodulated frequency ω_r) phase space (u, v) for blue detuned demodulation, $(\omega_r - \omega_0)/2\pi \approx 91$ Hz. (c) Several ringdown measurements in phase space for red detuned demodulation, $(\omega_r - \omega_0)/2\pi \approx -209$ Hz. (d) Reconstructed Hamiltonian for positive detuning, i.e., from measurements of panel (b), using Eq. (5). (e) Reconstructed Hamiltonian for negative detuning, i.e. from the measurements of panel (c).

in the definition of F . The parametric drive voltage amplitude U_p can be converted to a parametric modulation depth $\lambda = 2U_p/QU_{\text{th}}$ by measuring the parametric drive threshold amplitude $U_{\text{th}} \approx 1.98$ V. Above the parametric threshold, the system can be driven into an out-of-equilibrium stationary oscillation via a spontaneous time-translation symmetry breaking [4, 8, 37, 39–47]. The full device characterization is shown in Appendix A.

III. HAMILTONIAN RECONSTRUCTION

We now introduce our method for reconstructing the Hamiltonian from measured coordinates along a trajectory. The evolution of a classical lossless system in the laboratory frame with coordinate x and its conjugate p

is given by Hamilton's EOMs

$$\begin{aligned}\frac{dx}{dt} &= +\frac{\partial H(x,p)}{\partial p}, \\ \frac{dp}{dt} &= -\frac{\partial H(x,p)}{\partial x},\end{aligned}\quad (2)$$

where $H(x,p)$ is the Hamiltonian. Here, for any initial conditions and without drive, trajectories form closed loops along equipotential lines in coordinate space (x,p) since there is no energy loss. This means that only a single loop of the Hamiltonian can be sampled when following any given trajectory. To sample all potential elevations, one has to initialize the system at infinitely many different initial conditions.

In many cases, we are interested in the slowly-varying in-phase and out-of-phase quadratures $u(t)$ and $v(t)$ observed in a frame rotating at $\omega_r \approx \omega_0$, which are defined via $x(t) = u(t)\cos(\omega_r t) - v(t)\sin(\omega_r t)$. The demodulated quadrature we measure with our lock-in amplifier at frequency ω_r are precisely u and v . By applying the averaging method [48] on an equation of motion such as Eq. (1), we obtain the so-called slow-flow equations (see Appendix B). We open the system by adding dissipative terms $\propto \Gamma$, i.e., we consider rotating Lagrangian dynamics, such that the equations of motion can be formulated in a similar structure as Eqs. (2):

$$\begin{aligned}\frac{du}{dt} &= +\frac{\partial H_{\text{rot}}(u,v)}{\partial v} - \frac{\Gamma}{2}u, \\ \frac{dv}{dt} &= -\frac{\partial H_{\text{rot}}(u,v)}{\partial u} - \frac{\Gamma}{2}v.\end{aligned}\quad (3)$$

In this frame, the energy-conserving evolution of the system is governed by a rotating-frame quasi-Hamiltonian H_{rot} . For our resonator, subjected to both parametric and external drives, H_{rot} reads [49]

$$\begin{aligned}H_{\text{rot}} &= \frac{\omega_r^2 - \omega_0^2}{4\omega_r}(u^2 + v^2) \\ &\quad - \frac{3\beta}{32\omega_r}(2u^2v^2 + u^4 + v^4) \\ &\quad + \frac{\lambda\omega_0^2}{8\omega_r}(2uv\sin\psi + (u^2 - v^2)\cos\psi) \\ &\quad + \frac{AU_r}{2\omega_r}(u\cos\theta + v\sin\theta).\end{aligned}\quad (4)$$

This Hamiltonian H_{rot} is a function in the rotating phase space spanned by u and v [20], and is the quantity we reconstruct in this paper.

The addition of dissipation in Eq. (3) is crucial. In the presence of dissipation, a trajectory is no longer confined to a single closed loop, but samples different energy elevations, ending up in one of the stable stationary states of the system, see Fig. 1(b). This allows us to probe H_{rot} by experimentally measuring $u(t)$ and $v(t)$ using rotating-frame ringdown measurements. By initializing the system in an initial state (u_i, v_i) and letting it evolve

to a final state (u_f, v_f) , we can extract the change in the Hamiltonian ΔH_{rot} at any point (u_j, v_j) along this ringdown's trajectory. We isolate H_{rot} in Eqs. (3) and integrate over the slow coordinates from (u_i, v_i) to (u_j, v_j) to obtain

$$\Delta H_{\text{rot}} = \int_{v_i}^{v_j} \left[\frac{du}{dt} + \frac{\Gamma}{2}u \right] dv - \int_{u_i}^{u_j} \left[\frac{dv}{dt} + \frac{\Gamma}{2}v \right] du. \quad (5)$$

In practice, the values (u_j, v_j) are measured in discrete steps, allowing to compute ΔH_{rot} only at these points. Measuring multiple ringdowns with different initial (u_i, v_i) , ΔH_{rot} can be deterministically sampled and reconstructed over a large area of phase space, with a resolution limited by the measurement uncertainty or fluctuations (e.g. thermal or quantum noise) in u and v . Note that Eq. (5) does not provide the relative change of ΔH_{rot} between different ringdown measurements.

To compare different traces, we make use of the fact that $H_{\text{rot}}(u_f, v_f)$ should be single-valued at stationary points. This means that all traces sharing the same final coordinates (u_f, v_f) should have the same final value $H_{\text{rot}}(u_f, v_f)$. We thus find the relative Hamiltonian offset between different ringdown traces sharing the same (u_f, v_f) by comparing $H_{\text{rot}}(u_f, v_f)$. Finding the offset between traces is more complicated when they have different values of (u_f, v_f) , i.e., they do not share a common end point. Here, the offset can be calculated by making the Hamiltonian continuous, i.e. by finding the offset that minimizes the difference between nearby starting points (u_i, v_i) that decay into different final (u_f, v_f) , see Appendix C.

Note that a Hamiltonian reconstruction analogous to Eq. (5) can also be performed in the nonrotating frame, i.e., for a dissipative Eq. (2). We concentrate here on the case of a rotating-frame Hamiltonian to be in line with the theory. In the following, we will test the Hamiltonian reconstruction before discussing what information we can extract from it.

IV. HARMONIC OSCILLATOR CASE

As a first demonstration, we reconstruct the rotating-frame Hamiltonian of a damped harmonic oscillator. In Figs. 1(b) and (c), we show multiple measured trajectories for the case $\lambda = 0$, and with amplitudes that are small enough to neglect the effect of the Duffing nonlinearity, i.e. only considering the first line in Eq. (4). For each of those ringdown trajectories, we first displace the resonator in phase space using a near-resonant drive with fixed U_r and ω_r , and with an individually selected θ . In a frame rotating at ω_r , the corresponding initial resonator coordinates (u_i, v_i) , shown as dots, are stationary under the resonant drive. Then, we switch off the drive ($U_r = F = 0$), and track the ringdown trajectory while the system decays to the state $(u_f = 0, v_f = 0)$. During this decay, the angle of the state in phase space

evolves in time since the rotating frame's frequency is detuned from the resonance frequency [21]. For $\omega_r - \omega_0 > 0$ in Fig. 1(b), the trajectories spiral towards $(0, 0)$ with a clockwise orientation, while for $\omega_r - \omega_0 < 0$ in Fig. 1(c), they spiral in counterclockwise direction.

We reconstruct the rotating-frame Hamiltonian H_{rot} from the ringdown trajectories using Eq. (5). For the reconstructions in Fig. 1(d) and (e), the resolution was improved by using more ringdown traces than shown in Figs. 1(b) and (c). The resulting H_{rot} is a paraboloid whose sign of curvature depends on $\omega_r - \omega_0$. This is predicted in Eq. (4) and reflects the fact that H_{rot} describes energy relative to a rotating frame. Indeed, for $\omega_r - \omega_0 = 0$, the rotating potential would be entirely flat. Note that the origin $(0, 0)$, which appears as a maximum of H_{rot} in Fig. 1(e), remains the only stable solution of the system irrespective of the detuning. As a (local) maximum can appear as a stationary state, this example demonstrates that the rotating-frame Hamiltonian cannot be interpreted as a simple energy function as is the case in the non-rotating frame [48]. After successfully reconstructing the rotating frame potential of a harmonic oscillator, we now apply our method to a more complex system.

V. PARAMETRIC OSCILLATOR CASE

The reconstruction of H_{rot} can also be applied to driven nonlinear systems with multiple stable solutions. Here, we demonstrate this principle on the example of the electromechanical resonator described in Sec. II when subjected to a parametric drive, cf. Eq. (4) and Fig. 1(a).

We first analyze a single rotating-frame ringdown into an out-of-equilibrium stationary state in phase space. In Fig. 2, we study an example trajectory of our system in the presence of parametric driving beyond the instability threshold ($\lambda > \lambda_{\text{th}}$) [48], where two time-translation symmetry-broken high-amplitude solutions are stabilized due to the interplay between the drive and the nonlinearity, see Appendix A. As shown schematically in Fig. 2(a), the system is initialized in (u_i, v_i) by a near-resonant force at ω_r , followed by a parametric drive tone whose amplitude $\lambda \propto U_p$ and frequency $2\omega_r$ define the stationary solutions of the system in the readout frame rotating at frequency ω_r [48, 50, 51]. In Fig. 2(b), we show a typical ringdown trajectory of our resonator in phase space, noting that $(u_f \neq 0, v_f \neq 0)$.

To facilitate the Hamiltonian reconstruction, we define displaced quadratures $\tilde{u} \equiv u - u_f$ and $\tilde{v} \equiv v - v_f$, with the final coordinates of the ringdown (u_f, v_f) (i.e., the attractor position). In this shifted reference frame, the relaxation into the stable solution resembles a ringdown process in an equilibrium system, with \tilde{u} and \tilde{v} performing damped oscillations towards a final state ($\tilde{u}_f = 0, \tilde{v}_f = 0$), see Fig. 2(c)(i). The damping rate associated with these trajectories is quantified by the same Γ as we introduced in Eq. (1), while the rotation around (u_f, v_f) depends on

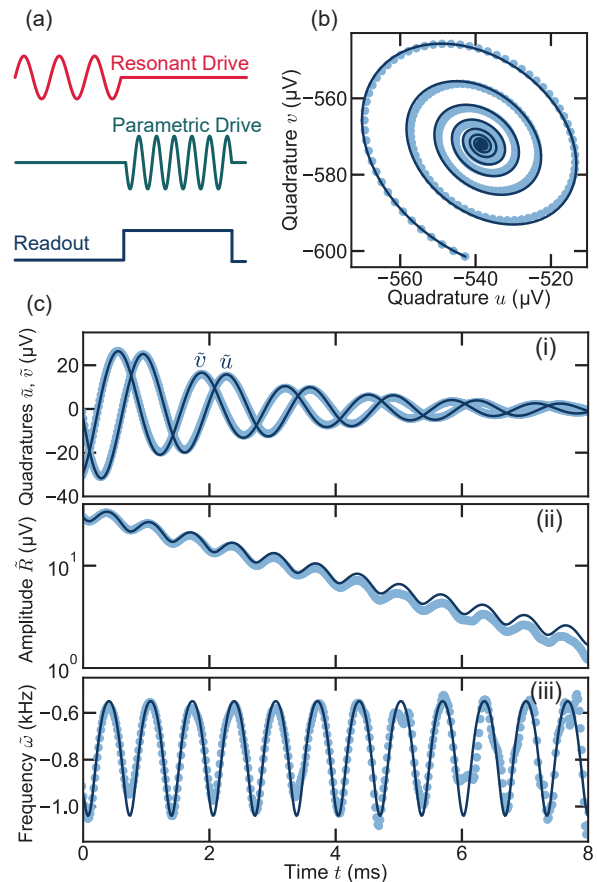


FIG. 2. Ringdown of a parametric oscillator. (a) For a ringdown measurement, the resonator is first displaced with a near-resonant drive $U_{\text{in}}(\omega_r)$ with $\omega_r \approx \omega_0$. This resonant drive is turned off and a parametric drive $U_{\text{in}}(2\omega_r)$ is immediately turned on, while the slowly-varying (i.e., demodulated at ω_r) quadratures u and v are read out. (b) Ringdown in phase space for fixed parametric drive $U_p = 10$ V ($\lambda \approx 10^{-3}$) and frequency $(\omega_r - \omega_0)/2\pi \approx -253$ Hz. The dark blue curve is the predicted ringdown with the linearized model in Appendix B [Eq. (B6)]. (c) In panels (i) the in-phase \tilde{u} and out-of-phase \tilde{v} displaced quadratures, (ii) amplitude $\tilde{R} = \sqrt{\tilde{u}^2 + \tilde{v}^2}$, and (iii) instantaneous rotating-frame frequency $\tilde{\omega} = \partial_t \tilde{\phi}/2\pi$ with phase $\tilde{\phi} = \arctan(\tilde{v}/\tilde{u})$ are plotted as a function of time for the same ringdown as in (b). These measurements are referenced to the attractor in which they ringdown into, i.e., $\tilde{u} \equiv u - u_f$ with $u_f \approx -538$ μV the final value of u (the position of the attractor), and similarly for \tilde{v} with $v_f \approx -572$ μV .

H_{rot} . The dynamics of these shifted quadratures are well captured by linearizing the equations of motion [Eqs. (3)] around the attractors, see derivation in Appendix B.

In contrast to undriven relaxation processes in the lab frame (x, p) , the amplitude $\tilde{R} = \sqrt{\tilde{u}^2 + \tilde{v}^2}$ does not decay monotonically. Instead, we observe oscillations imposed on top of the exponential decay in Fig. 2(c)(ii). These oscillations stem from the fact that the shape of H_{rot} around (u_f, v_f) is not rotationally symmetric, such that the system samples different $\partial_u H_{\text{rot}}$ and $\partial_v H_{\text{rot}}$ as

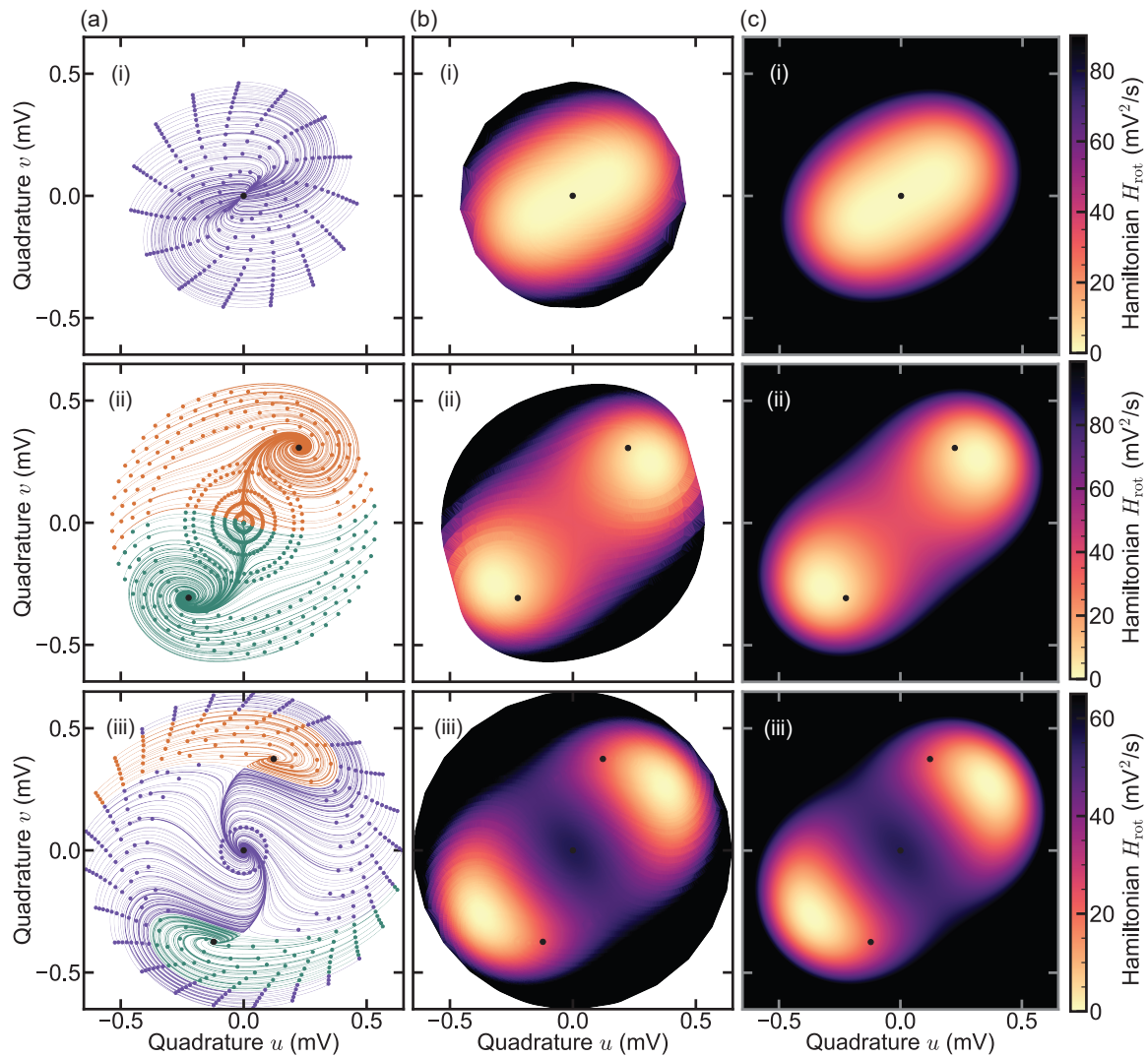


FIG. 3. Ringdowns and Hamiltonian reconstruction in parametric phase space. (a) Multiple ringdowns in phase space under different parametric drive strength and frequency. Each ringdown's starting point is indicated by a dot, and color-coded for the attractor in which it rings down: purple the zero-amplitude, orange the top-right, and green the bottom-left attractor. The attractors extracted from the ringdown measurements are indicated by black dots. The parametric drive is (i) below threshold, (ii) above threshold, and (iii) above threshold and far detuned, cf. Appendix A for the locations of the measurements relative to the device's phase diagram. (b) Rotating-frame Hamiltonian reconstruction from the ringdown measurements in (a), cf. Eq. (5). (c) Theoretical plots of the rotating-frame Hamiltonian [Eq. (4)] using potential angle (i) $\psi \approx -2.1$ rad, (ii) $\psi \approx -1.76$ rad, and (iii) $\psi \approx -1.86$ rad as the only fit parameter, while fixing the independently measured mechanical parameters, see Appendix A. Note that the attractors are not necessarily at the minima of the quasi-Hamiltonian due to dissipation.

it moves around the Hamiltonian landscape. We emphasize that despite the fact that we observe oscillations growing in amplitude at certain times, this does not violate any law of conservation, as we are dealing with a driven system. The non-rotationally symmetric Hamiltonian also manifests in Fig. 2(c)(iii), where an instantaneous rotating-frame frequency $\tilde{\omega} = \partial_t \tilde{\phi} / 2\pi$ is defined by the phase $\tilde{\phi} = \arctan(\tilde{v}/\tilde{u})$ relative to the attractor.

There are clear oscillations in the frequency $\tilde{\omega}$ due to the resonator sampling different $\partial_u H_{\text{rot}}$ and $\partial_v H_{\text{rot}}$ as it moves in phase space. This behavior is also well captured by the averaged and linearized dynamics near the

attractors (cf. Eqs. (3) and Appendix B). Note that for smaller parametric drives or for dynamics further away from the attractors, one needs to consider a model that goes beyond the linearization we employ (i.e. expand the equations to higher-order terms) to fully capture the dynamics.

In a next step, we measure multiple trajectories with various initialization conditions, but fixed parametric drive strength and frequency, allowing us to reconstruct the rotating frame Hamiltonian H_{rot} of our driven nonlinear system. In Fig. 3(a), we show such sets of trajectories for three different parametric drives: (i) below threshold

with a single squeezed state, (ii) above threshold with two stable phase states, and (iii) at large driving and large detuning with a combination of phase states and a zero-amplitude state (see Appendix A for a phase diagram of the device). Each ringdown is color-coded by the state it eventually approaches, allowing us to identify the corresponding attractor pools. From ringdown measurements, we can thus directly identify the number of stable solutions in the given phase-space area, as well as the separatrices of the system – the regions where the color of nearby ringdown measurements changes. In addition, we obtain a visualization of the stream flow in phase space, as governed by Eq. (3). We stress that the main assumption of this reconstruction is that the damping is linear, cf. Eqs. (3), though these equations could be adapted to include other types of damping. The reconstruction does not assume linearized dynamics.

The reconstructed Hamiltonians H_{rot} are shown in Fig. 3(b) alongside theoretical Hamiltonians in Fig. 3(c), as calculated from Eq. (4) with independently measured parameters ω_0 , β , and λ , see Appendix A. We find excellent qualitative agreement between measurement and theory. Crucially, the quality and resolution of the Hamiltonian reconstruction is consistently high over the entire sampled phase space, which would be hard to achieve with statistical methods [6–13]. In the reconstructed H_{rot} , we can clearly see the appearance of one, two, and three stable states in the three cases (i)–(iii), respectively, indicating different phases of the driven system [27, 28, 52]. Our reconstruction method confirms the theoretical prediction that the stationary solutions can qualitatively differ in the rotating frame; while the phase states at finite amplitude in the cases (ii) and (iii) are marked by a minimum in H_{rot} , the stable state appearing at $(u = 0, v = 0)$ in (iii) corresponds to a maximum, signalling a fundamentally different type of solution, i.e., a dissipation-stabilized state [29, 30]. In the following, we analyze this difference using the symplectic norm of the individual solutions, and we show that this quantity yields valuable insights into the behavior of driven-dissipative systems.

VI. SYMPLECTIC NORM

In sections IV and V, we successfully reconstructed rotating-frame Hamiltonians H_{rot} using ringdown measurements. One of the most prominent distinctions of a rotating-frame Hamiltonian, compared with a Hamiltonian in a laboratory frame such as in Eq. (2), is that both maxima and minima of H_{rot} can constitute stable oscillation states of the system, unlike what we expect from the minimal action principle in equilibrium systems. This counter-intuitive feature can be clearly observed in row (iii) of Fig. 3, where two minima at finite amplitudes are separated by a stable local maximum at $(u = v = 0)$. Importantly, the minima in Fig. 3 are stable due to the nonlinearity β , while the maximum is stabilized by dis-

sipation [30]. This fundamental difference, however, is difficult to quantify in standard measurements, such as frequency sweeps and stability diagrams [41, 53].

A method tailored to classify and distinguish minima and maxima in H_{rot} is the symplectic norm ds^2 [29, 30]. This quantity indicates if the excitations (i.e., out-of-equilibrium phonons) of a system around an attractor are more hole-like or particle-like: when an excitation with a negative (positive) symplectic norm is created on top of a stationary system, it reduces (increases) the energy of the system relative to the rotating frame, that is, relative to an excitation at the driving frequency ω_r . This difference manifests in the Hamiltonian: stationary solutions with a negative (positive) symplectic norm appear as maxima (minima) in H_{rot} and are formally associated with a hole-like (particle-like) excitation, see Appendix B. We can therefore use the reconstructed Hamiltonians in Fig. 3 to directly determine the symplectic norm of the stable oscillations states, and to classify the corresponding excitations.

A careful study of Fig. 3 reveals additional information. Namely, the trajectories leading to Hamiltonian extrema assume clockwise or counter-clockwise rotations. For our system, we show in Appendix B that the symplectic norm is directly linked to the sense of rotation of the trajectories close to an attractor. This allows us to extract the symplectic norm ds^2 of the different attractors directly from the measured ringdown trajectories, even without a full reconstruction. To capture this observation mathematically, we define a correlator characterizing the direction of rotation of a ringdown,

$$G^c(t' - t) = \Theta(t' - t) \langle \tilde{v}(t) \tilde{u}(t') - \tilde{u}(t) \tilde{v}(t') \rangle_t, \quad (6)$$

with the Heavyside step-function $\Theta(t - t')$, and $\langle \dots \rangle_t$ indicating an average over all times t . This quantity $G^c(t - t')$ is a classical analogue to the quantum Green's function used in Refs. [30, 34, 54]. Following these works, we calculate the corresponding spectral response \mathcal{A} of a stable oscillation state

$$\begin{aligned} \mathcal{A}(\omega) &= -2\text{Im}[G^c(\omega)] \\ &= \frac{|\zeta|^2 ds^2}{2} \left[\frac{1}{(\omega - \omega_{\text{lin}})^2 + \frac{\Gamma^2}{4}} - \frac{1}{(\omega + \omega_{\text{lin}})^2 + \frac{\Gamma^2}{4}} \right], \end{aligned} \quad (7)$$

where $G^c(\omega)$ is the Fourier transform of $G^c(t - t')$, ζ is a constant related to the ringdown starting conditions, and ω_{lin} is the oscillation frequency of the quadratures. The linear response function in the second line is only valid near the attractor of interest.

Looking at \mathcal{A} , we see that the spectral response has peaks at $\pm\omega_{\text{lin}}$, with width Γ , and an overall sign which is determined by the symplectic norm ds^2 . Therefore, if the resonator rings down with a counter-clockwise (clockwise) rotation in phase space, the final steady state of the system has a negative (positive) symplectic norm and a negative (positive) peak in \mathcal{A} .

With this knowledge, we can extract the sign of ds^2 from the spectral response of ringdown measurements,

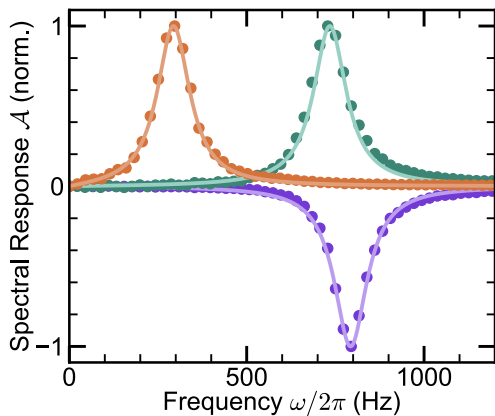


FIG. 4. Spectral response of a parametric oscillator. With \tilde{u} and \tilde{v} obtained during a ringdown measurement, we can extract the spectral response \mathcal{A} using Eqs. (6) and (7) (dots) [cf. Figs. (2) and (3)]. These spectral responses are in good agreement with the fitted theoretical curves of Eq. (7), with ω_0 left as a free parameter to account for small frequency drifts. All measurements are done with the same parametric drive strength $U_p = 10$ V ($\lambda \approx 10^{-4}$), and different demodulation frequencies ω_r . The detuning is $(\omega_r - \omega_0)/2\pi = 170$ Hz (orange) and $(\omega_r - \omega_0)/2\pi = -222$ Hz (green) for ring-downs into high amplitude states, and $(\omega_r - \omega_0)/2\pi = -865$ Hz (purple) for the zero amplitude state.

as shown in Fig. 4. We record \tilde{u} and \tilde{v} during one trajectory, calculate the correlator $G^c(t - t')$ [Eq. (6)], take its Fourier transform, and compute the spectral response \mathcal{A} according to Eq. (7). In Fig. 4, we present the measured result for each of the three stable states of a parametric oscillator at different detunings. We compare these measured spectral responses with those expected from theory, calculated using independently measured parameters and the linearized slow-flow equations [Eq. (7)], and obtain very good agreement. As expected, for a stable solution corresponding to a maximum in H_{rot} (purple curve), the spectral response is a dip, while the two other solutions, which are minima in H_{rot} (orange and green curves), correspond to peaks in the spectral response. These measurements show the link between the orientation of rotation, the symplectic norm, the spectral function, and the rotating frame Hamiltonian H_{rot} .

We emphasize that the notion of maxima and minima of the rotating quasienergy potential depend on the chosen rotating frame frequency, and that stabilized maxima are a manifestation of out-of-equilibrium stationary states. As such, the fact that the excitations on top of the maxima are hole-like implies that their dynamics are slower than the clock in the rotating frame as manifested by the chirality of their ringdown. In other words, we can think of the response in this case as non-causal relative to the clock. This is analogous to how antiparticles, that exhibit a negative mass dispersion, behave in relativistic quantum mechanics [55].

VII. OUTLOOK

We report a precise method to reconstruct the Hamiltonian of a system via ringdown measurements. The method allows for a full characterization of the energy potential, including multiple stable solutions, saddle points, and attractor pools. The method is particularly suited for studies in the growing field of driven-dissipative nonlinear systems, where a Hamiltonian characterization from first principles is often very difficult. Furthermore, it bestows the ability to characterize the symplectic norm of different stable oscillation solutions in the rotating frame with a connection to relativistic quantum mechanics and causality. We expect that this approach will allow the classification of a broad variety of systems, including nanomechanics, superconducting circuits, light-matter systems, and nonlinear optics.

ACKNOWLEDGEMENTS

We acknowledge Christian Marti and Sebastián Guerrero for help building the measurement setup. We thank Nicholas E. Bousse and T. W. Kenny for providing the MEMS device, and Matteo Fadel and Tobias Donner for useful discussions. V. D. acknowledges support from the ETH Zurich Postdoctoral Fellowship Grant No. 23-1 FEL-023. O. Z. acknowledges funding from the Deutsche Forschungsgemeinschaft (DFG) via project number 449653034 and through SFB143. A. E. and O. Z. acknowledge financial support from the Swiss National Science Foundation (SNSF) through the Sinergia Grant No. CRSII5_206008/1.

Appendix A: Experimental Characterization

1. Parametric Sweeps

In this section, we describe how we measure the parametric response of our resonator in order to extract its resonance frequency ω_0 , energy decay rate Γ , and Duffing nonlinearity β .

We send a parametric tone $U_{\text{in}} = U_p \cos(2\omega_r t)$ to our device and read out the induced displacement at frequency ω_r . In Fig. 5(a), we show the system's response while sweeping the frequency of the parametric drive from high to low frequencies for fixed parametric drive voltage $U_p = 4.54$ V. By repeating this measurement for different parametric drive voltages, we obtain the ‘phase diagram’ of our parametric oscillator, shown in Fig. 5(b). Now, performing the same measurement but instead sweeping the frequency from low to high frequencies (i.e., “against” the Duffing nonlinearity), we obtain a different diagram commonly referred to as ‘Arnold Tongue’, shown in Fig. 5(c).

Comparing with theoretical predictions [48], Figs. 5(b) and (c) allow us to read out the different phases and num-

ber of solutions of our resonator depending on the parametric drive strength and frequency. Indeed, the outline of the Arnold tongue, shown as a red dashed line, indicates the (frequency-dependent) parametric threshold, above which the resonator has exactly two stable states (the parametric phase states), both of which have finite-amplitude but opposite phases. The orange region outside the Arnold tongue in Fig. 5(b) features a zero-amplitude state in addition to the two parametric phase states. Which state is selected depends on the initial condition of the resonator. Finally, in the white region in Fig. 5(b) only the zero-amplitude state is stable.

To find the equation predicting the parametric response of our device, we use the ‘slow-flow’ equations [cf. Eqs. (3) and (B1)], and find the steady state amplitude response $R = \sqrt{u^2 + v^2}$ by setting $\dot{u} = \dot{v} = 0$, yielding [48]

$$\left[-\frac{\lambda^2}{4} + \left(\frac{\Gamma\omega}{\omega_0^2} \right)^2 + \left(1 - \frac{\omega^2}{\omega_0^2} + \frac{3\beta R^2}{4\omega_0^2} \right)^2 \right] R^2 = 0. \quad (\text{A1})$$

Equation (A1) has the trivial solution $R = 0$. For the case $R \neq 0$, we can divide Eq. (A1) by R^2 to obtain the non-trivial solutions

$$R(\omega) = \left(\frac{4\omega_0^2}{3\beta} \left[\left(\frac{\omega^2}{\omega_0^2} - 1 \right) \pm \left(\frac{\lambda^2}{4} - \frac{\Gamma^2\omega^2}{\omega_0^4} \right)^{1/2} \right] \right)^{1/2}, \quad (\text{A2})$$

when the radicands of both square roots are positive. Thus, the parametric amplitude response allows (amongst other things) to extract the Duffing nonlinearity.

The outline of the Arnold tongue corresponds to the limit $R \rightarrow 0$ in Eq. (A2), leading to

$$(\omega^2 - \omega_0^2)^2 - \frac{\lambda^2\omega_0^4}{4} + \Gamma^2\omega^2 = 0. \quad (\text{A3})$$

Solving for the parametric drive yields

$$\lambda = 2\sqrt{\frac{\Gamma^2\omega^2}{\omega_0^4} + \left(1 - \frac{\omega^2}{\omega_0^2} \right)^2}, \quad (\text{A4})$$

where we kept the (physical) positive solution.

To extract our device parameters, we start by fitting Eq. (A4) to the outline of the Arnold tongue, see red dashed line in Fig. 5(c). For the fit, we replace $\lambda = U_p/C$, where C is a constant converting the unitless parametric drive strength λ to the applied parametric voltage U_p . Doing so, we obtain the resonance frequency $\omega_0/2\pi = 1.1198294(3)$ MHz and the energy decay rate $\Gamma/2\pi = 112(2)$ Hz of our resonator, as well as the conversion constant $C = 9.88(5) \times 10^3$ V.

In a second step, we use the measured parametric response in Fig. 5(a) and fit it to Eq. (A2) in order to extract the Duffing nonlinearity $\beta = -9.894(4) \times 10^{16}$ (V·s)⁻², while fixing ω_0 , Γ , and C to the previously fitted values.

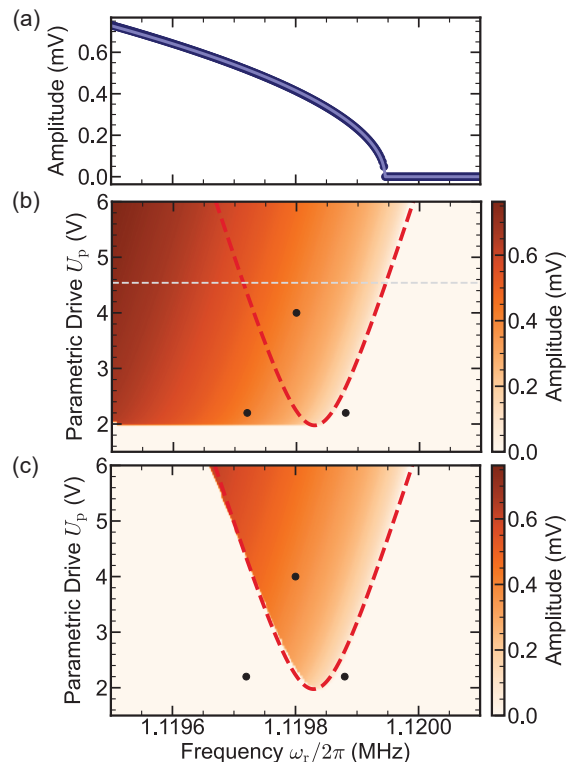


FIG. 5. Parametric response. (a) Response of our resonator to a parametric drive $U_{\text{in}} = U_p \cos(2\omega_r t)$ with voltage amplitude $U_{\text{in}} = 4.54$ V. The frequency is swept from high to low values. (b) Response to a parametric drive as in (a) for different values of U_p . The dashed grey line indicates the measurement of panel (a), the red dashed line corresponds to the fitted ‘Arnold tongue’ outline [see panel (c)], while the dots indicate the parameters used in Fig. 3. (c) Response to a parametric drive as in (a) for different values of U_p when sweeping from low to high frequencies.

2. Resonant Sweep

We now extract the factor A , converting from an input voltage $U_{\text{in}} = U_r \cos(\omega_r t)$ to an applied force F (in units Vs⁻²), from the resonant response of our resonator.

To calibrate this, we consider the EOM for our resonator under near-resonant (but small, i.e., neglecting the Duffing term) drive [cf. Eq. (1)],

$$\ddot{x}(t) + \omega_0^2 x(t) + \Gamma \dot{x}(t) = AU_{\text{in}}(t), \quad (\text{A5})$$

where we replaced the forcing term by $F = AU_{\text{in}}$. Taking the Fourier transform of Eq. (A5) yields

$$x(\omega) = AU_{\text{in}}(\omega) [\omega_0^2 - \omega^2 - i\omega\Gamma]^{-1}, \quad (\text{A6})$$

which provides a direct link between the voltage U_{in} applied to our device and the voltage $U_{\text{out}} \equiv x$ we read out.

We can thus extract A by sweeping the frequency ω_r of a driving tone across the mechanical resonance of our resonator and measuring its response. In Fig. 6, we fit

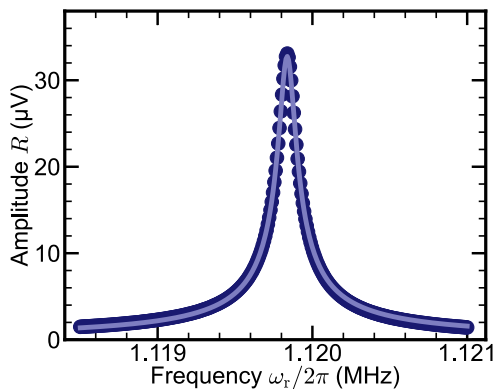


FIG. 6. Linear resonant response. An input voltage $U_{\text{in}} = U_r \cos(\omega_r t)$ with $U_r = 10$ mV is swept across the resonance frequency and the amplitude response $R = \sqrt{u^2 + v^2}$ at frequency ω_r is measured (dots). The data is fitted (line) according to Eq. (A6) with fixed $\Gamma/2\pi = 112$ Hz, while ω_0 is left as a free parameter to account for small frequency drifts. We extract a value $A = 16.22(1) \times 10^6 \text{ s}^{-2}$.

the measured response with Eq. (A6) and obtain $A = 16.22(1) \times 10^6 \text{ s}^{-2}$.

Appendix B: Linearized Model

In this Appendix, we describe the method we use to obtain the EOMs for the rotating frame coordinates u and v , and the link between the symplectic norm and the ringdown trajectories. We first obtain the steady state solutions under parametric drive, then we linearize the EOMs in their vicinity. We solve the linearized EOMs to get analytical expressions for the resonators rotation frequency and direction around the attractors. The latter reveals a direct link between the ringdown rotation and

the symplectic norm of the corresponding final steady state. Finally, we show how to extract the symplectic norm from a ringdown measurement using the spectral response function.

1. Averaging Method

As described in the main text, starting from Eq. (1), we move to a rotating frame with out-of-phase quadratures $u(t)$ and $v(t)$, defined via $x(t) = u(t) \cos(\omega_r t) - v(t) \sin(\omega_r t)$. Assuming that $u(t)$ and $v(t)$ vary slowly in time compared to the mechanical oscillations with frequency ω_r , we average the EOMs over the time $2\pi/\omega_r$ to obtain approximated EOMs for $u(t)$ and $v(t)$ [48],

$$\begin{aligned} \dot{u} &= -\frac{\Gamma}{2}u - \delta v - \frac{3\beta}{8\omega_r}(u^2v + v^3) - \frac{\lambda\omega_0^2}{4\omega_r}v, \\ \dot{v} &= -\frac{\Gamma}{2}v + \delta u + \frac{3\beta}{8\omega_r}(u^3 + uv^2) - \frac{\lambda\omega_0^2}{4\omega_r}u, \end{aligned} \quad (\text{B1})$$

where we introduce the detuning $\delta \equiv (\omega_0^2 - \omega_r^2)/2\omega_r$. For simplicity, we also set $\psi = 0$ when moving from Eq. (1) to Eq. (B1). This phase ψ rotates the potential in phase space around the origin with an angle of $\psi/2$, so the solutions for u or v calculated for $\psi = 0$ in this section can be rotated by an angle of $\psi/2$ to match the experimental results.

2. Linearization of the EOMs

To predict the motion of the resonator near an attractor, we linearize the slow-flow equations [Eqs. (B1)] near the attractors [48, 56]. To do so, we first determine the coordinates of the attractors (i.e., the stationary states of the system) in the rotating frame by setting $\dot{u} = \dot{v} = 0$ in Eq. (B1). Solving the resulting coupled polynomial equations leads to five possible solutions [57, 58]:

$$\begin{aligned} (u_f, v_f)_1 &= (0, 0), \\ (u_f, v_f)_{2,3} &= \left(\pm u_+, \pm \frac{u_+(3\beta\lambda\omega_0^2 u_+^2 - 2\lambda^2\omega_0^4 + 4\Gamma^2\omega_r^2 + 4\lambda\omega_0^4 - 4\lambda\omega_0^2\omega_r^2)}{2\Gamma\omega_r(2\omega_r^2 - 2\omega_0^2 + \lambda\omega_0^2)} \right), \\ (u_f, v_f)_{4,5} &= \left(\pm u_-, \pm \frac{u_-(3\beta\lambda\omega_0^2 u_-^2 - 2\lambda^2\omega_0^4 + 4\Gamma^2\omega_r^2 + 4\lambda\omega_0^4 - 4\lambda\omega_0^2\omega_r^2)}{2\Gamma\omega_r(2\omega_r^2 - 2\omega_0^2 + \lambda\omega_0^2)} \right), \end{aligned} \quad (\text{B2})$$

where

$$u_{\pm} = \left[\frac{\beta\lambda\omega_0^2(2\lambda\omega_0^2\omega_r^2 + \lambda^2\omega_0^4 - 2\lambda\omega_0^4 - 4\Gamma^2\omega_r^2) \pm \sqrt{\beta^2\lambda^2\omega_0^4(2\omega_r^2 - 2\omega_0^2 + \lambda\omega_0^2)^2(\lambda^2\omega_0^4 - 4\Gamma^2\omega_r^2)}}{3\beta^2\lambda^2\omega_0^4} \right]^{1/2}. \quad (\text{B3})$$

For any given set of parameters, a maximum of three of these solutions are stable, i.e., they act as attractors, cf.

Fig. 3. To see if a solution is stable, we now introduce

the displaced quadratures $(\tilde{u}, \tilde{v})_k \equiv (u - u_f, v - v_f)_k$, relative to a given solution position $(u_f, v_f)_k$, and linearize Eq. (B1) around one attractor by neglecting higher-order terms in \tilde{u} and \tilde{v} . This procedure yields

$$\begin{pmatrix} \dot{\tilde{u}} \\ \dot{\tilde{v}} \end{pmatrix} = \underbrace{\begin{pmatrix} \frac{\partial \dot{u}}{\partial u} & \frac{\partial \dot{u}}{\partial v} \\ \frac{\partial \dot{v}}{\partial u} & \frac{\partial \dot{v}}{\partial v} \end{pmatrix}}_{\mathbf{J}_f} \bigg|_{(u,v)=(u_f,v_f)_k} \begin{pmatrix} \tilde{u} \\ \tilde{v} \end{pmatrix}. \quad (\text{B4})$$

Here, \mathbf{J}_f is the Jacobian of the slow-flow equations evaluated around the solution position $(u_f, v_f)_k$, which takes the form

$$\mathbf{J}_f = \begin{pmatrix} -\frac{\Gamma}{2} - \frac{3\beta u_f v_f}{4\omega_f} & -\delta - \frac{3\beta(u_f^2 + 3v_f^2)}{8\omega_r} - \frac{\lambda\omega_0^2}{4\omega_r} \\ \delta + \frac{3\beta(3u_f^2 + v_f^2)}{8\omega_r} - \frac{\lambda\omega_0^2}{4\omega_r} & -\frac{\Gamma}{2} + \frac{3\beta u_f v_f}{4\omega_r} \end{pmatrix}. \quad (\text{B5})$$

The Jacobian \mathbf{J}_f describes the linearized forces acting in the rotating frame near a given solution. Solving the linear first-order differential equation given by Eq. (B4) leads to

$$\begin{pmatrix} \tilde{u} \\ \tilde{v} \end{pmatrix} = \zeta \mathbf{w}_+ e^{\mu_+ t} + \zeta^* \mathbf{w}_- e^{\mu_- t}. \quad (\text{B6})$$

Here,

$$\zeta = \frac{1}{2}(v_i - v_f) - i \left(\frac{3\beta u_f v_f}{8\omega_r \omega_{\text{lin}}} (v_i - v_f) + \frac{(9\beta u_f^2 + 3\beta v_f^2 + 4\omega_0^2 - 4\omega_r^2 - 2\lambda\omega_0^2)}{16\omega_r \omega_{\text{lin}}} (u_i - u_f) \right) \quad (\text{B7})$$

is a constant which depends on the initial position (u_i, v_i) of the resonator in the rotating frame. Furthermore, we use in Eq. (B6) the Jacobian's eigenvectors

$$\mathbf{w}_{\pm} = \begin{pmatrix} \frac{-6\beta u_f v_f \pm 8i\omega_r \omega_{\text{lin}}}{9\beta u_f^2 + 3\beta v_f^2 + 4\omega_0^2 - 4\omega_r^2 - 2\lambda\omega_0^2} \\ 1 \end{pmatrix}, \quad (\text{B8})$$

and corresponding eigenvalues

$$\mu_{\pm} = -\Gamma/2 \pm i\omega_{\text{lin}}, \quad (\text{B9})$$

with the complex frequency

$$\omega_{\text{lin}} = \frac{1}{8\omega_r} \left[27\beta^2 u_f^4 + 6\beta u_f^2 (9\beta v_f^2 + 8\omega_0^2 - 8\omega_r^2 + 2\lambda\omega_0^2) + (3\beta v_f^2 + 4\omega_0^2 - 4\omega_r^2 - 2\lambda\omega_0^2) \times (9\beta v_f^2 + 4\omega_0^2 - 4\omega_r^2 + 2\lambda\omega_0^2) \right]^{1/2}. \quad (\text{B10})$$

If the real part of one eigenvalue in Eq. (B9) is positive, Eq. (B6) diverges for $t \rightarrow \infty$ and $(u_f, v_f)_k$ is an unstable state. If both real parts are negative, (\tilde{u}, \tilde{v}) converge to $(0, 0)$ and $(u_f, v_f)_k$ is an attractor [48, 56]. The theory results depicted in Fig. 2(b), (c)(i), and (c)(ii) are directly calculated using Eq. (B6).

The theory prediction for the frequency of the rotation around an attractor in Fig. 2(c)(iii) is analytically calculated using

$$\begin{aligned} \frac{1}{2\pi} \frac{d\tilde{\phi}}{dt} &= \frac{\partial}{\partial t} \arctan \left(\frac{\tilde{v}}{\tilde{u}} \right) \\ &= \frac{1}{2\pi} \frac{\tilde{u}(d\tilde{v}/dt) - \tilde{v}(d\tilde{u}/dt)}{\tilde{u}^2 + \tilde{v}^2} \\ &= -\frac{|\zeta|^2 \omega_{\text{lin}}}{\pi} \frac{ds^2}{\tilde{u}^2 + \tilde{v}^2} e^{-\Gamma t}, \end{aligned} \quad (\text{B11})$$

with the ‘symplectic norm’ defined as

$$ds^2 \equiv i(w_{+,1}w_{-,2} - w_{-,1}w_{+,2}), \quad (\text{B12})$$

and where $w_{\pm,l}$ is the l -th entry of \mathbf{w}_{\pm} . The sign of ds^2 therefore decides the rotational sense of the ring-down. We now show that this quantity is identical to the symplectic norm derived for quantum driven-dissipative systems, which allows to classify stable states in driven-dissipative systems [29, 30, 59].

3. Symplectic Norm

To see that the symplectic norm [cf. Eq. (B12)] is the same as the one defined in quantum driven-dissipative systems, we transform our definition of the symplectic norm to the form commonly used in quantum optics [29, 30, 59]. First, we express the rotating frame coordinates $\tilde{u}(t)$ and $\tilde{v}(t)$ in terms of the complex coordinate $\alpha(t)$ and its complex conjugate $\alpha^*(t)$ via the transformation matrix \mathbf{S} :

$$\begin{pmatrix} \tilde{u} \\ \tilde{v} \end{pmatrix} = \underbrace{\sqrt{\frac{\hbar}{2m\omega_0}} \begin{pmatrix} 1 & 1 \\ i & -i \end{pmatrix}}_{\equiv \mathbf{S}^{-1}} \begin{pmatrix} \alpha \\ \alpha^* \end{pmatrix}. \quad (\text{B13})$$

This basis change can be interpreted as moving to the mean-field limit of bosonic creation and annihilation operators of a quantum harmonic oscillator representing the quadratures $\tilde{u}(t)$ and $\tilde{v}(t)$ (i.e., $\alpha = \langle a \rangle$ with a bosonic annihilation operator a and expectation value $\langle \dots \rangle$).

Note that the $\sqrt{\hbar/2m\omega_0}$ prefactor is the same for both quadratures due to our definition of \tilde{u} and \tilde{v} sharing the same units. This prefactor leads to

$$\mathbf{S}^{-1} = \frac{\hbar}{m\omega_0} \mathbf{S}^\dagger, \quad (\text{B14})$$

implying that \mathbf{S} is not unitary and therefore not a norm-preserving transformation. This will later be accounted for by scaling the vectors in the new basis, and has no consequences for the sign of the symplectic norm, which is the relevant quantity for us.

We use the transformation introduced in Eqs. (B4)

and (B13) to find the equations of motion for α and α^* :

$$\begin{aligned} i\mathbf{S} \begin{pmatrix} \dot{\tilde{u}} \\ \dot{\tilde{v}} \end{pmatrix} &= i\mathbf{S}\mathbf{J}_f \begin{pmatrix} \tilde{u} \\ \tilde{v} \end{pmatrix} \\ \Rightarrow i \begin{pmatrix} \dot{\alpha} \\ \dot{\alpha}^* \end{pmatrix} &= \underbrace{i\mathbf{S}\mathbf{J}_f\mathbf{S}^{-1}}_{\equiv \mathbf{D}} \begin{pmatrix} \alpha \\ \alpha^* \end{pmatrix}. \end{aligned} \quad (\text{B15})$$

We multiplied both sides of Eq. (B13) with a complex factor i in order to bring Eq. (B15) into a form where the so-called dynamic matrix \mathbf{D} [60] of the system can be directly read out. This is crucial as the symplectic norm defined in Ref. [30] is formulated in terms of the eigenvectors of the dynamic matrix.

The eigenvectors \mathbf{v}_\pm of the dynamic matrix \mathbf{D} can be calculated using the eigenvectors \mathbf{w}_\pm of the Jacobian \mathbf{J}_f :

$$\begin{aligned} \mathbf{J}_f\mathbf{w}_\pm &= \mu_\pm\mathbf{w}_\pm \\ \Rightarrow i\mathbf{S}\mathbf{J}_f\mathbf{S}^{-1}\mathbf{S}\mathbf{w}_\pm &= i\mu_\pm\mathbf{S}\mathbf{w}_\pm \\ \Rightarrow i\mathbf{D}\mathbf{S}\mathbf{w}_\pm &= i\mu_\pm\mathbf{S}\mathbf{w}_\pm \\ \Rightarrow \mathbf{D} \left(\sqrt{\frac{m\omega_0}{\hbar}}\mathbf{v}_\pm \right) &= i\mu_\pm \left(\sqrt{\frac{m\omega_0}{\hbar}}\mathbf{v}_\pm \right). \end{aligned} \quad (\text{B16})$$

In the last line, we used the definition of \mathbf{D} from Eq. (B15) and introduced an additional factor of $\sqrt{m\omega_0/\hbar}$ to ensure that $|\mathbf{w}_\pm| = |\mathbf{v}_\pm|$, accounting for the fact that \mathbf{S} is not a unitary transformation, cf. Eq. (B14).

Since $\mathbf{w}_+ = \mathbf{w}_+^*$, this implies that $\mathbf{v}_+ = \mathbf{v}_+^*$, and we have $\mathbf{w}_+^\dagger = \mathbf{w}_+^T$, as well as $\mathbf{v}_+^\dagger = \mathbf{v}_+^T$ (with T denoting transpose), allowing us to rewrite the classical symplectic norm defined in Eq. B12 as

$$\begin{aligned} ds^2 &= (w_{-,1}, w_{-,2}) \begin{pmatrix} 0 & -i \\ i & 0 \end{pmatrix} \begin{pmatrix} w_{+,1} \\ w_{+,2} \end{pmatrix} \\ &= (w_{-,1}, w_{-,2}) \mathbf{S}^\dagger (\mathbf{S}^\dagger)^{-1} \begin{pmatrix} 0 & -i \\ i & 0 \end{pmatrix} \mathbf{S}^{-1}\mathbf{S} \begin{pmatrix} w_{+,1} \\ w_{+,2} \end{pmatrix} \\ &= (\mathbf{S}\mathbf{w}_+)^{\dagger} (\mathbf{S}^\dagger)^{-1} \begin{pmatrix} 0 & -i \\ i & 0 \end{pmatrix} \mathbf{S}^{-1}\mathbf{S}\mathbf{w}_+ \\ &= \mathbf{v}_+^{\dagger} \mathbf{I}_- \mathbf{v}_+, \end{aligned} \quad (\text{B17})$$

with $\mathbf{I}_- = \text{diag}(1, -1)$, and where we used $\mathbf{v}_+ = \mathbf{S}\mathbf{w}_+$. Since the symplectic norm is real valued, one could also calculate it using \mathbf{v}_- , yielding the same result:

$$ds^2 = (ds^2)^\dagger = \left(\mathbf{v}_+^{\dagger} \mathbf{I}_- \mathbf{v}_+ \right)^\dagger = \mathbf{v}_-^{\dagger} \mathbf{I}_- \mathbf{v}_-. \quad (\text{B18})$$

Equations (B17) and (B18) show that the (classical) symplectic norm defined in Eq. (B12) coincides exactly with the symplectic norm introduced in Ref. [30]. As the sign of Eq. (B11) is determined by ds^2 , the rotational sense of a ringdown is directly linked with the sign of the symplectic norm of the attractor. Since the sign of the symplectic norm of an attractor is positive (negative) for a minimum (maximum) of the underlying potential [29, 30], the rotational sense of the ringdown can be used to differ between maxima and minima in the rotating frame potential.

4. Spectral Response

Having established a link between the rotational sense of ringdowns and the symplectic norm, we derive the ‘spectral response’ of fluctuations around an attractor. This spectral response also allows us to extract the symplectic norm from ringdown measurements.

In analogy to driven-dissipative quantum systems [29, 30], we first introduce the correlator function

$$\begin{aligned} G^c(t' - t) &= \Theta(t' - t) (\tilde{v}(t)\tilde{u}(t') - \tilde{u}(t)\tilde{v}(t'))_t \\ &= \Theta(t' - t) \frac{2ds^2|\zeta|^2}{\Gamma} e^{-\frac{\Gamma}{2}(t'-t)} \sin(\omega_{\text{lin}}(t' - t)), \end{aligned} \quad (\text{B19})$$

where ‘cc.’ denotes the complex conjugate, and $\Theta(t - t')$ is the Heavyside step-function. The function G^c correlates the displaced quadratures $\tilde{u}(t)$ and $\tilde{v}(t')$ at different times to capture the rotational sense of a ringdown near an attractor. This correlator is reminiscent of Eq. (B12), and is analogous to a retarded Green’s function in driven-dissipative quantum systems, correlating at different times the creation and annihilation of bosons on top of a stable solution. Note that the second equality in Eq. (B19) holds in the limit of the linearization procedure presented earlier.

The sign of the symplectic norm can now be read out directly by inspecting the peaks and dips of the spectral function [29, 30, 34]. This spectral response is related to the imaginary part of the Fourier transform of the Green’s function $G^c(\omega)$ via

$$\mathcal{A}(\omega) = -2\text{Im}[G^c(\omega)]. \quad (\text{B20})$$

Explicitly computing Eq. (B20) using Eq. (B19) yields the spectral response of our system:

$$\mathcal{A}(\omega) = \frac{|\zeta|^2 ds^2}{2} \left[\frac{1}{(\omega - \omega_{\text{lin}})^2 + \frac{\Gamma^2}{4}} - \frac{1}{(\omega + \omega_{\text{lin}})^2 + \frac{\Gamma^2}{4}} \right]. \quad (\text{B21})$$

A peak (dip) of \mathcal{A} at positive frequencies therefore corresponds to a positive (negative) symplectic norm and hence to a minimum (maximum) of the rotating frame potential H_{rot} at (u_f, v_f) .

Appendix C: Details of the Hamiltonian Reconstruction

In this section, we provide further details on the Hamiltonian reconstruction process. We start the reconstruction by using a single ringdown measurement with the quadratures $u_j(t_j)$ and $v_j(t_j)$ measured at discrete times t_j . Assuming that our device is linearly damped, and using the extracted damping Γ , we calculate the change in the Hamiltonian $\Delta H_{\text{rot}}(u_j, v_j)$ at each coordinates along the ringdown path by numerically integrating Eq. (5).

We then find the attractor k , e.g. $k = 1, 2, 3$ for the case of three attractors, in which the resonator rings

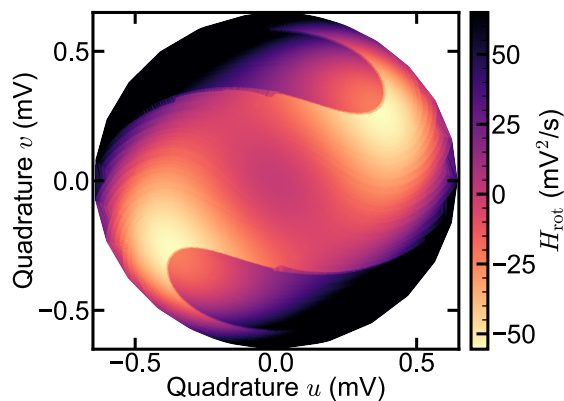


FIG. 7. Hamiltonian reconstruction before adjusting the offset C_k of each attractor. After using Eq. (5) to recover the relative Hamiltonian potential along each ringdown trajectory and setting the end point of each ringdown to $C_k = 0$, we obtain a discontinuous Hamiltonian. The clear discontinuity happens at the separatrix of the system since the offset between the different attractors $C_k - C_{k+1}$ has yet to be found.

down into by looking at the final value $(u_f, v_f)_k$. We fix the Hamiltonian $H_{\text{rot}}(u_f, v_f) = C_k$ at the final coordinate $(u_f, v_f)_k$ to an arbitrary value C_k . To do so, we add a constant offset to the Hamiltonian change ΔH_{rot} calculated

for the ringdown. This will insure that the Hamiltonian is single-valued at each attractor, i.e., $H_{\text{rot}}(u_f, v_f)$ is the same for each ringdown ending up in the same attractor. At this stage, we simply set $C_k = 0$.

As a second step, we repeat the integration procedure for all ringdown measurements and check if the final value of each ringdown $(u_f, v_f)_k$ is the same as the first ringdown, or if it ends up at another attractor. If it is another attractor, we label the new attractor as $k + 1$, and add an arbitrary value C_{k+1} to the trace, which we will later adjust. We repeat this procedure for all measured ringdowns, allowing to find the Hamiltonian change for all the ringdown paths, as shown in Fig. 7 for an example with three attractors.

We generally find discontinuities in the Hamiltonian reconstruction at the separatrices between different attractors, see Fig. 7. Such discontinuities are unphysical and stem from our choice to set all offsets to $C_k = 0$. As a last step of the reconstruction, we thus need to find the relative height $C_k - C_{k+1}$ between the attractors such that the discontinuities disappear. In practice, we fix one of the constants (e.g., $C_1 = 0$), and vary the constant offsets C_k of the other attractors (C_2 and C_3 in Fig. 7) until the Hamiltonian is smooth (i.e., such that the second differentials of H_{rot} with respect to u and v are minimized). We furthermore set the minimum of $H_{\text{rot}} = 0$, yielding Fig. 3(a)(iii). For our demonstration examples, this optimization was done manually.

-
- [1] M. T. Cuairan, J. Gieseler, N. Meyer, and R. Quidant, “Precision calibration of the duffing oscillator with phase control,” *Phys. Rev. Lett.* **128**, 213601 (2022).
- [2] E. Bairey, I. Arad, and N. H. Lindner, “Learning a local hamiltonian from local measurements,” *Phys. Rev. Lett.* **122**, 020504 (2019).
- [3] X.-L. Qi and D. Ranard, “Determining a local hamiltonian from a single eigenstate,” *Quantum* **3**, 159 (2019).
- [4] Z. Lin, K. Inomata, K. Koshino, W. D. Oliver, Y. Nakamura, J. S. Tsai, and T. Yamamoto, “Josephson parametric phase-locked oscillator and its application to dispersive readout of superconducting qubits,” *Nature Commu.* **5**, 4480 (2014).
- [5] K. Siva, G. Koolstra, J. Steinmetz, W. P. Livingston, D. Das, L. Chen, J. Kreikebaum, N. Stevenson, C. Jünger, D. Santiago, I. Siddiqi, and A. Jordan, “Time-dependent hamiltonian reconstruction using continuous weak measurements,” *PRX Quantum* **4**, 040324 (2023).
- [6] E. Florin, A. Pralle, E. Stelzer, and J. Hörber, “Photonic force microscope calibration by thermal noise analysis,” *Appl. Phys. A* **66**, S75 (1998).
- [7] L. I. McCann, M. Dykman, and B. Golding, “Thermally activated transitions in a bistable three-dimensional optical trap,” *Nature* **402**, 785 (1999).
- [8] H. B. Chan and C. Stambaugh, “Activation barrier scaling and crossover for noise-induced switching in micromechanical parametric oscillators,” *Phys. Rev. Lett.* **99**, 060601 (2007).
- [9] S. Jeney, E. H. Stelzer, H. Grubmüller, and E.-L. Florin, “Mechanical properties of single motor molecules studied by three-dimensional thermal force probing in optical tweezers,” *ChemPhysChem* **5**, 1150 (2004).
- [10] Y. Tanaka, S. Kaneda, and K. Sasaki, “Nanostructured potential of optical trapping using a plasmonic nanoblock pair,” *Nano Lett.* **13**, 2146 (2013).
- [11] L. Rondin, J. Gieseler, F. Ricci, R. Quidant, C. Delgado, and L. Novotny, “Direct measurement of kramers turnover with a levitated nanoparticle,” *Nat. Nanotechnol.* **12**, 1130 (2017).
- [12] N. Zijlstra, D. Nettel, R. Satija, D. E. Makarov, and B. Schuler, “Transition path dynamics of a dielectric particle in a bistable optical trap,” *Phys. Rev. Lett.* **125**, 146001 (2020).
- [13] A. Militaru, M. Innerbichler, M. Frimmer, F. Tebbenjohanns, L. Novotny, and C. Dellago, “Escape dynamics of active particles in multistable potentials,” *Nat. Comm.* **12**, 2446 (2021).
- [14] P. Wu, R. Huang, C. Tischer, A. Jonas, and E.-L. Florin, “Direct measurement of the nonconservative force field generated by optical tweezers,” *Phys. Rev. Lett.* **103**, 108101 (2009).
- [15] L. Pérez García, J. Donlucas Pérez, G. Volpe, A. V. Arzola, and G. Volpe, “High-performance reconstruction of microscopic force fields from brownian trajectories,” *Nat. Comm.* **9**, 5166 (2018).
- [16] T. L. Heugel, R. Chitra, A. Eichler, and O. Zilberberg, “Proliferation of unstable states and their impact on stochastic out-of-equilibrium dynamics,”

- arXiv:2307.13718 (2023).
- [17] P. Álvarez, D. Pittilini, F. Miserocchi, S. Raamamurthy, G. Margiani, O. Ameye, J. del Pino, O. Zilberberg, and A. Eichler, “A biased ising model using two coupled kerr parametric oscillators with external force,” arXiv:2307.13676 (2023).
- [18] B. Swingle, “Unscrambling the physics of out-of-time-order correlators,” *Nat. Phys.* **14**, 988 (2018).
- [19] P. D. Blocher, S. Asaad, V. Mourik, M. A. I. Johnson, A. Morello, and K. Mølmer, “Measuring out-of-time-ordered correlation functions without reversing time evolution,” *Phys. Rev. A* **106**, 042429 (2022).
- [20] A. Bachtold, J. Moser, and M. I. Dykman, “Mesoscopic physics of nanomechanical systems,” *Rev. Mod. Phys.* **94**, 045005 (2022).
- [21] T. Antoni, K. Makles, R. Braive, T. Briant, P.-F. Cochadon, I. Sagnes, I. Robert-Philip, and A. Heidmann, “Nonlinear mechanics with suspended nanomembranes,” *EPL* **100**, 68005 (2012).
- [22] P. M. Polunin, Y. Yang, M. I. Dykman, T. W. Kenny, and S. W. Shaw, “Characterization of mems resonator nonlinearities using the ringdown response,” *J. Microelectromechanical Syst.* **25**, 297 (2016).
- [23] L. Catalini, M. Rossi, E. C. Langman, and A. Schliesser, “Modeling and observation of nonlinear damping in dissipation-diluted nanomechanical resonators,” *Phys. Rev. Lett.* **126**, 174101 (2021).
- [24] A. Morales, P. Zupancic, J. Léonard, T. Esslinger, and T. Donner, “Coupling two order parameters in a quantum gas,” *Nat. Mater.* **17**, 686 (2018).
- [25] I. Kozinsky, H. C. Postma, O. Kogan, A. Husain, and M. L. Roukes, “Basins of attraction of a nonlinear nanomechanical resonator,” *Phys. Rev. Lett.* **99**, 207201 (2007).
- [26] Y. Yan, X. Dong, L. Huang, K. Moskovtsev, and H. Chan, “Energy transfer into period-tripled states in coupled electromechanical modes at internal resonance,” *Phys. Rev. X* **12**, 031003 (2022).
- [27] J. Woo and R. Landauer, “Fluctuations in a parametrically excited subharmonic oscillator,” *IEEE J. Quantum Electron* **7**, 435 (1971).
- [28] M. I. Dykman, C. M. Maloney, V. N. Smelyanskiy, and M. Silverstein, “Fluctuational phase-flip transitions in parametrically driven oscillators,” *Phys. Rev. E* **57**, 5202 (1998).
- [29] M. Soriente, R. Chitra, and O. Zilberberg, “Distinguishing phases using the dynamical response of driven-dissipative light-matter systems,” *Phys. Rev. A* **101**, 023823 (2020).
- [30] M. Soriente, T. L. Heugel, K. Omiya, R. Chitra, and O. Zilberberg, “Distinctive class of dissipation-induced phase transitions and their universal characteristics,” *Phys. Rev. Res.* **3**, 023100 (2021).
- [31] F. Ferri, R. Rosa-Medina, F. Finger, N. Dogra, M. Soriente, O. Zilberberg, T. Donner, and T. Esslinger, “Emerging dissipative phases in a superradiant quantum gas with tunable decay,” *Phys. Rev. X* **11**, 041046 (2021).
- [32] A. Roy, S. Jahani, C. Langrock, M. Fejer, and A. Marandi, “Spectral phase transitions in optical parametric oscillators,” *Nat. Comm.* **12**, 835 (2021).
- [33] G.-Q. Zhang, Z. Chen, W. Xiong, C.-H. Lam, and J. Q. You, “Parity-symmetry-breaking quantum phase transition via parametric drive in a cavity magnonic system,” *Phys. Rev. B* **104**, 064423 (2021).
- [34] O. Scarlatella, A. A. Clerk, and M. Schiro, “Spectral functions and negative density of states of a driven-dissipative nonlinear quantum resonator,” *New J. Phys.* **21**, 043040 (2019).
- [35] M. Agarwal, S. A. Chandorkar, H. Mehta, R. N. Candler, B. Kim, M. A. Hopcroft, R. Melamud, C. M. Jha, G. Bahl, G. Yama, T. W. Kenny, and B. Murmann, “A study of electrostatic force nonlinearities in resonant microstructures,” *Appl. Phys. Lett.* **92**, 104106 (2008).
- [36] S. Schmid, L. G. Villanueva, and M. L. Roukes, *Fundamentals of nanomechanical resonators*, Vol. 49 (Springer, 2016).
- [37] J. M. Miller, D. D. Shin, H.-K. Kwon, S. W. Shaw, and T. W. Kenny, “Phase control of self-excited parametric resonators,” *Phys. Rev. Applied* **12**, 044053 (2019).
- [38] Ž. Nosan, P. Märki, N. Hauff, C. Knaut, and A. Eichler, “Gate-controlled phase switching in a parametron,” *Phys. Rev. E* **99**, 062205 (2019).
- [39] M. Marthaler and M. I. Dykman, “Switching via quantum activation: A parametrically modulated oscillator,” *Phys. Rev. A* **73**, 042108 (2006).
- [40] D. Ryvkine and M. I. Dykman, “Resonant symmetry lifting in a parametrically modulated oscillator,” *Phys. Rev. E* **74**, 061118 (2006).
- [41] I. Mahboob and H. Yamaguchi, “Bit storage and bit flip operations in an electromechanical oscillator,” *Nat. Nanotechnol.* **3**, 275 (2008).
- [42] C. M. Wilson, T. Duty, M. Sandberg, F. Persson, V. Shumeiko, and P. Delsing, “Photon generation in an electromagnetic cavity with a time-dependent boundary,” *Phys. Rev. Lett.* **105**, 233907 (2010).
- [43] A. Leuch, L. Papariello, O. Zilberberg, C. L. Degen, R. Chitra, and A. Eichler, “Parametric symmetry breaking in a nonlinear resonator,” *Phys. Rev. Lett.* **117**, 214101 (2016).
- [44] J. Gieseler, B. Deutsch, R. Quidant, and L. Novotny, “Subkelvin parametric feedback cooling of a laser-trapped nanoparticle,” *Phys. Rev. Lett.* **109**, 103603 (2012).
- [45] A. Grimm, N. E. Frattini, S. Puri, S. O. Mundhada, S. Touzard, M. Mirrahimi, S. M. Girvin, S. Shankar, and M. H. Devoret, “Stabilization and operation of a kerr-cat qubit,” *Nature* **584**, 205 (2020).
- [46] Z. Wang, M. Pechal, E. A. Wollack, P. Arrangoiz-Arriola, M. Gao, N. R. Lee, and A. H. Safavi-Naeini, “Quantum dynamics of a few-photon parametric oscillator,” *Phys. Rev. X* **9**, 021049 (2019).
- [47] T. Yamaji, S. Kagami, A. Yamaguchi, T. Satoh, K. Koshino, H. Goto, Z. R. Lin, Y. Nakamura, and T. Yamamoto, “Spectroscopic observation of the crossover from a classical duffing oscillator to a kerr parametric oscillator,” *Phys. Rev. A* **105**, 023519 (2022).
- [48] A. Eichler and O. Zilberberg, *Classical and Quantum Parametric Phenomena* (Oxford University Press, 2023).
- [49] Note that H_{rot} may not have dimensions of energy in this notation because u and v have the same units. The quasi-Hamiltonian can be expressed in units of energy by changing $H_{\text{rot}} \rightarrow H_{\text{rot}}/m\omega_r$ in Eqs. (3) and (4).
- [50] M. C. Lifshitz, R. Cross, “Nonlinear dynamics of nanomechanical and micromechanical resonators,” in *Reviews of Nonlinear Dynamics and Complexity* (Wiley, 2009) pp. 1–52.
- [51] M. Dykman, *Fluctuating Nonlinear Oscillators* (Oxford

- University Press, 2012).
- [52] M.-S. Heo, Y. Kim, K. Kim, G. Moon, J. Lee, H.-R. Noh, M. I. Dykman, and W. Jhe, “Ideal mean-field transition in a modulated cold atom system,” *Phys. Rev. E* **82**, 031134 (2010).
- [53] R. Karabalin, S. Masmanidis, and M. Roukes, “Efficient parametric amplification in high and very high frequency piezoelectric nanoelectromechanical systems,” *Appl. Phys. Lett.* **97**, 183101 (2010).
- [54] M. Soriente, T. Donner, R. Chitra, and O. Zilberberg, “Dissipation-induced anomalous multicritical phenomena,” *Phys. Rev. Lett.* **120**, 183603 (2018).
- [55] P. A. M. Dirac, “Relativistic quantum mechanics,” *Proc. R. Soc. Lond. A* **136**, 453 (1932).
- [56] H. J. Ricardo, *A Modern Introduction to Differential Equations (Third Edition)*, edited by H. J. Ricardo (Academic Press, 2021) pp. 361–420.
- [57] J. Kořata, J. del Pino, T. L. Heugel, and O. Zilberberg, “HarmonicBalance.jl: A Julia suite for nonlinear dynamics using harmonic balance,” *SciPost Phys. Codebases*, 6 (2022).
- [58] V. Borovik, P. Breiding, J. del Pino, M. Michałek, and O. Zilberberg, “Khovanskii bases for semimixed systems of polynomial equations – approximating stationary nonlinear newtonian dynamics,” *J. Math. Pures Appl.* **182**, 195 (2024).
- [59] J. Fan and S. Jia, “Collective dynamics of the unbalanced three-level dicke model,” *Phys. Rev. A* **107**, 033711 (2023).
- [60] M. Xiao, “Theory of transformation for the diagonalization of quadratic hamiltonians,” arXiv:0908.0787 (2009).